Journal of
Applied Crystallography

ISSN 0021-8898

Received 7 March 2013
Accepted 4 July 2013

Insight into neutron focusing: the out-of-focus condition

B. Hammouda,[a]* D. F. R. Mildner,[a] A. Brûlet[b] and S. Desert[b]

[a]Center for Neutron Research, National Institute of Standards and Technology, 100 Bureau Drive, Building 235, Gaithersburg, MD 20899-6102, USA, and [b]Laboratoire Léon Brillouin, UMR12 CEA-CNRS, CE Saclay, 91191 Gif sur Yvette, France. Correspondence e-mail: hammouda@nist.gov

Neutron focusing leads to significant gains in flux-on-sample in small-angle neutron scattering and very small angle neutron scattering instruments. Understanding the out-of-focus condition is necessary for less than optimal conditions such as for short instruments and low neutron wavelengths. Neutron focusing is investigated using a three-pronged approach. The three methods are analytical calculations, resolution measurements and computer simulations. A source aperture containing a single small-size hole and a sample aperture containing multiple holes are used to produce multiple spots on the high-resolution neutron detector. Lens focusing elongates off-axis spots in the radial direction. The standard deviation for the size of each spot is estimated using these three approaches. Varying parameters include the neutron wavelength, the number of focusing lenses and the location of holes on the sample aperture. Enough agreement for the standard deviation of the individual neutron beams was found between the calculations and the measurements to give confidence in this approach. Good agreement was found between the standard deviations obtained from calculations and simulations as well. Excellent agreement was found for the mean location of these individual spots.

1. Introduction

The resolution function and the minimum scattering variable $Q_{\min}$ are well understood for small-angle neutron scattering (SANS) instruments (Mildner & Carpenter, 1984). In order to enhance flux-on-sample, neutron focusing is often used on SANS instruments. Neutron focusing lenses are used to concentrate the neutron beam, thereby lowering $Q_{\min}$. The use of biconcave lenses allows the opening up of the sample aperture without too much loss in instrumental resolution (Gähler *et al.*, 1980; Eskildsen *et al.*, 1998; Choi *et al.*, 2000; Mildner, 2005, 2005). The variance of the SANS resolution function comprises geometric contributions (corresponding to the source aperture, sample aperture and detector resolution terms) as well as the wavelength spread contribution term. Gravity effects become important at longer wavelengths. The effects of neutron focusing lenses and gravity-correcting prisms have been modeled and compared with neutron optics measurements (Hammouda & Mildner, 2007). Neutron focusing investigations are usually undertaken in the focusing condition whereby the neutron spot size on the detector is the smallest possible. This is done by adjusting the neutron wavelength for a fixed (maximum reachable) sample-to-detector distance and for the required number of lenses. When the optimal focusing condition cannot be reached (for example, when the focusing wavelength is too high or in order to keep a low number of lenses in the beam) then operating in an out-of-focus condition is necessary. The present investigations concentrate on the out-of-focus condition. The standard deviation of the resolution function is derived for this condition and tested experimentally.

Very small angle neutron scattering (VSANS) instruments can achieve lower $Q_{\min}$ resolution by using multiple (individual) holes on the source and sample apertures and a host of additional apertures in between in order to avoid cross collimation between holes. In addition, VSANS instruments use high-resolution neutron detectors in order to minimize the instrumental resolution and $Q_{\min}$. Neutron focusing is also desired on VSANS instruments. We have conducted neutron focusing optics measurements on a VSANS instrument (the TPA spectrometer at LLB, Saclay, France) and compared the results with the neutron focusing formalism that we now develop as well as with ray tracing Monte Carlo simulations.

2. Out-of-focus condition

The standard parameters are first defined: L_1 and L_2 are the source-to-sample and sample-to-detector distances, r_1 and r_2 are the source and sample aperture (individual holes) radii, respectively, Δx_3 and Δy_3 are the detector cell sizes, λ and $\Delta\lambda$ are the neutron wavelength and wavelength spread, and N is the number of biconcave lenses stacked along the neutron beam path (at the sample position), each with a radius of curvature R. The focal length of the lens is given by $f = R/2N(1 - n)$; here n is the lens refractive index, which can

be expressed in terms of the lens density ρ and scattering length b as $n = 1 - \rho b\lambda^2/2\pi$.

In the out-of-focus condition, the image of the source aperture is located at a distance L_4 from the sample aperture (Fig. 1). Note that $L_2 = L_4$ only in the focusing condition; in general, $L_2 \neq L_4$ for any out-of-focus condition. Simple geometrical optics states the following relationship: $1/f = 1/L_1 + 1/L_4$. The previous relations can be combined as

$$\frac{\pi}{\rho b}\frac{R}{N\lambda^2} = \frac{L_1 L_4}{L_1 + L_4}. \quad (1)$$

Note that, for MgF_2 lenses, $\rho b/\pi = 1.632 \times 10^{-6}$ Å^{-2}, so that

$$\frac{N\lambda^2}{R}\left(\frac{L_1 L_4}{L_1 + L_4}\right) = \frac{\pi}{\rho b} = 6.13 \times 10^5 \text{ Å}^2. \quad (2)$$

In addition, $f = (\pi/\rho b)(R/N\lambda^2)$, so that the focal length depends inversely on the square of the neutron wavelength.

The in-focus condition is characterized by

$$\frac{1}{f_0} = \frac{1}{L_1} + \frac{1}{L_2} = \frac{2N}{R}\frac{\rho b}{2\pi}\lambda_0^2. \quad (3)$$

λ_0 is the optimum focusing wavelength $\lambda_0 = [(1/N) \times (\pi/\rho b)\, R(L_1 + L_2)/L_1 L_2]^{1/2}$ (for which the neutron spot has a minimum size) and f_0 is the in-focus focal length.

This out-of-focus condition yields an equation with f_0 replaced by f and λ_0 replaced by λ. Here λ is any neutron wavelength (*i.e.* the actual wavelength used when the focusing wavelength λ_0 is prohibitively long) and f is the focal length corresponding to λ.

Fig. 2 shows the optics for the out-of-focus condition for a system that is focused at a distance L_4 and a wavelength λ, but with the detector located at L_2. It was shown (Mildner *et al.*, 2005) that the geometric contribution of the variance of the spatial resolution function for the out-of-focus condition in the horizontal direction is given by

$$\left[\sigma_x^2\right]_{\text{geo}} = \left(\frac{L_2}{L_4}\right)^2 \frac{r_4^2}{4} + \left(\frac{L_4 - L_2}{L_4}\right)^2 \frac{r_2^2}{4} + \frac{1}{3}\left(\frac{\Delta x_3}{2}\right)^2. \quad (4)$$

Here r_4 is the image of the source aperture, given by $r_4 = (L_4/L_1)r_1$. Noting that

$$\frac{1}{f_0} - \frac{1}{f} = \frac{1}{L_2} - \frac{1}{L_4} = \frac{L_4 - L_2}{L_2 L_4} = \frac{1}{f_0}\left[1 - \left(\frac{\lambda}{\lambda_0}\right)^2\right], \quad (5)$$

one obtains

$$\left[\sigma_x^2\right]_{\text{geo}} = \left(\frac{L_2}{L_1}\right)^2 \frac{r_1^2}{4} + \left(\frac{L_1 + L_2}{L_1}\right)^2 S(\lambda, \lambda_0)\frac{r_2^2}{4} + \frac{x_3^2}{12}. \quad (6)$$

The chromatic aberrations function $S(\lambda, \lambda_0)$ is obtained by averaging the factor $[1 - (\lambda/\lambda_0)^2]^2$ over the triangular wavelength distribution. The result is

$$S(\lambda, \lambda_0) = \left[1 - \left(\frac{\lambda}{\lambda_0}\right)^2\right]^2 + \left(\frac{\Delta\lambda}{\lambda}\right)^2 \left(\frac{\lambda}{\lambda_0}\right)^2 \left[\left(\frac{\lambda}{\lambda_0}\right)^2 - \frac{1}{3}\right] + \frac{1}{15}\left(\frac{\lambda}{\lambda_0}\right)^4 \left(\frac{\Delta\lambda}{\lambda}\right)^4. \quad (7)$$

The last term is negligible. The no-lens condition is recovered by verifying that $S(\lambda, \lambda_0 \to \infty) = 1$. The in-focus condition (*i.e.* when $\lambda = \lambda_0$) is also recovered as $S(\lambda \to \lambda_0) = (2/3)(\Delta\lambda/\lambda)^2 = 4(\sigma_\lambda/\lambda)^2$, where $\sigma_\lambda^2 = (1/6)\Delta\lambda^2$ is the variance of the triangular wavelength distribution.

In the vertical direction, the effect of gravity adds another term containing the same average over the wavelength distribution:

$$\left[\sigma_y^2\right]_{\text{geo}} = \left(\frac{L_2}{L_1}\right)^2 \frac{r_1^2}{4} + \left(\frac{L_1 + L_2}{L_1}\right)^2 S(\lambda, \lambda_0)\frac{r_2^2}{4} + \frac{\Delta y_3^2}{12} + A^2\lambda^4 4\left(\frac{\sigma_\lambda}{\lambda}\right)^2. \quad (8)$$

A is the familiar gravity correction factor given by $A = L_2(L_1 + L_2)gm^2/2h^2$, where g is the acceleration due to gravity, m is the neutron mass and h is Planck's constant. Since our interest in these investigations is in the spot size of the direct beam, no finite scattering variable term is included (i.e. $Q = 0$ is assumed throughout). Moreover, this approach considers one (individual) hole for the source aperture and one (individual) hole for the sample aperture only. The case of multiple (individual) holes on the sample aperture is considered next.

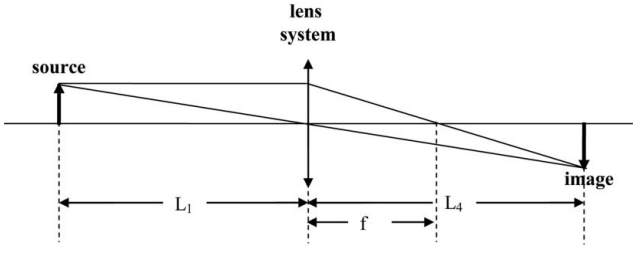

Figure 1
Simple optics shows how the image of a source is obtained using a focusing lens system for a wavelength λ.

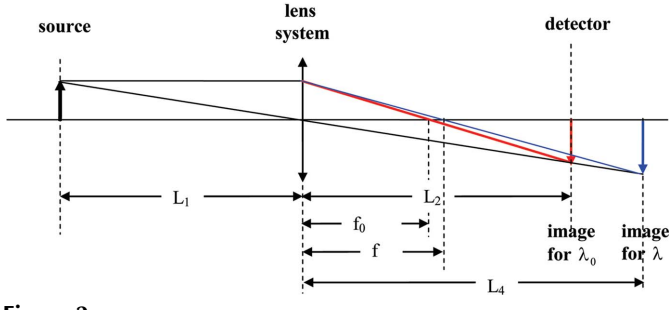

Figure 2
Optics for the out-of-focus condition.

3. Off-axis beam condition

Consider one single hole on the source aperture and an array of (individual) holes on the sample aperture (Fig. 3). The individual holes are located at positions $\{n_x a_x, n_y a_y\}$, where n_x and n_y are integers and a_x and a_y are the center-to-center inter-hole distances. The central hole corresponds to $n_x = n_y = 0$. For any off-axis beam (passing through an off-axis hole) on the sample aperture, chromatic aberrations distort the neutron beam spot on the detector so that it becomes stretched in the radial (also referred to as the parallel) direction. The perpendicular (or tangential) direction is not affected by this distortion (see Fig. 4).

For off-axis holes along the horizontal (x) axis, the variances in the radial (σ_{xr}^2) and perpendicular (σ_{xp}^2) directions are

$$\begin{aligned}\sigma_{xr}^2 &= \left[\sigma_x^2\right]_{\rm geo} + \left[2n_x a_x\left(1+\frac{L_2}{L_1}\right)\left(\frac{\lambda}{\lambda_0}\right)^2\right]^2\left(\frac{\sigma_\lambda}{\lambda}\right)^2,\\ \sigma_{xp}^2 &= \left[\sigma_x^2\right]_{\rm geo} + \left(2A\lambda^2\right)^2\left(\frac{\sigma_\lambda}{\lambda}\right)^2.\end{aligned} \tag{9}$$

The second term containing $n_x a_x$ is based on the observation that shifting the lens system horizontally shifts the image on the detector by a proportional amount but in the opposite direction (Mildner *et al.*, 2005).

For off-axis holes along the vertical (y) axis, the variances are

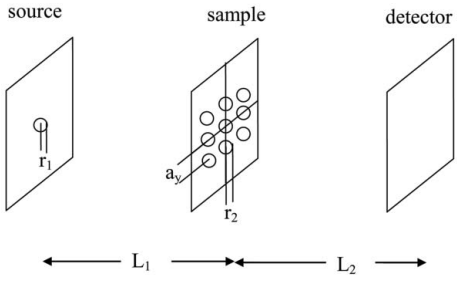

Figure 3
A schematic showing the source and sample apertures and the detector plane. This figure is not to scale.

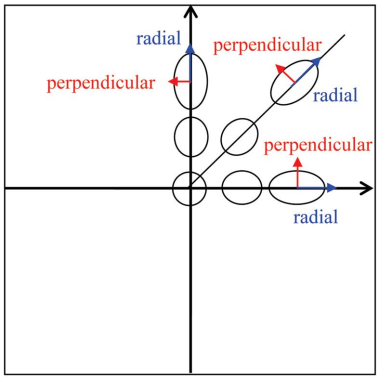

Figure 4
Schematic representation of the distorted neutron beam spots on the detector for off-axis holes on the sample aperture and focusing lenses in the out-of-focus condition.

$$\begin{aligned}\sigma_{yr}^2 &= \left[\sigma_y^2\right]_{\rm geo} + \left[2A\lambda^2 + 2n_y a_y\left(1+\frac{L_2}{L_1}\right)\left(\frac{\lambda}{\lambda_0}\right)^2\right]^2\left(\frac{\sigma_\lambda}{\lambda}\right)^2,\\ \sigma_{yp}^2 &= \left[\sigma_y^2\right]_{\rm geo}.\end{aligned} \tag{10}$$

The geometric variances $[\sigma_x^2]_{\rm geo}$ and $[\sigma_y^2]_{\rm geo}$ are given in the previous section.

Holes on the sample aperture with arbitrary coordinates $\{n_x a_x, n_y a_y\}$ in Cartesian coordinates correspond to $\{(n_x^2 a_x^2 + n_x^2 a_x^2)^{1/2}, \varphi\}$ in polar coordinates. For the sake of completeness, the radial and perpendicular variances for such arbitrary location holes are included here:

$$\begin{aligned}\sigma_{\rm r}^2 &= \left[\sigma_{\rm r}^2\right]_{\rm geo} + \Big[2A\lambda^2\sin(\varphi)\\ &\quad + 2(n_x^2 a_x^2 + n_y^2 a_y^2)^{1/2}\left(1+\frac{L_2}{L_1}\right)\left(\frac{\lambda}{\lambda_0}\right)^2\Big]^2\left(\frac{\sigma_\lambda}{\lambda}\right)^2,\\ \sigma_{\rm p}^2 &= \left[\sigma_{\rm r}^2\right]_{\rm geo} + \left[2A\lambda^2\cos(\varphi)\right]^2\left(\frac{\sigma_\lambda}{\lambda}\right)^2,\end{aligned} \tag{11}$$

where

$$\begin{aligned}\cos(\varphi) &= n_x a_x/(n_x^2 a_x^2 + n_y^2 a_y^2)^{1/2},\\ \sin(\varphi) &= n_y a_y/(n_x^2 a_x^2 + n_y^2 a_y^2)^{1/2}.\end{aligned} \tag{12}$$

The formalism developed here will be applied next to neutron optics measurements performed on the VSANS (called TPA) instrument at Saclay.

4. Neutron focusing tests

Many neutron scattering facilities have built or are in the process of building VSANS instruments. These will permit the probing of nanostructures well into the micrometre range. Neutron focusing on VSANS will help widen the breadth of research to include weakly scattering samples such as dilute polymer or protein solutions.

The VSANS instrument at Saclay is a medium-length high-resolution instrument that can achieve a low $Q_{\rm min}$ ($\sim$0.0003 Å^{-1}) ordinarily using multiple individual holes on the source and sample apertures, along with a high-resolution ($\sim$0.15 mm) image-plate neutron detector (the mar345).

In order to minimize gamma background on the image plate, the instrument uses two neutron supermirrors (instead of a conventional velocity selector) for monochromation so that the line of direct sight from the neutron source is blocked. This produces a neutron beam with discrete usable wavelengths of 6, 9.1, 12.34 and 14.59 Å, with a wavelength spread of $\Delta\lambda/\lambda = 0.15$ (Désert *et al.*, 2007). Details of instrumental conditions are included in Appendix *A*.

In its normal operating condition, this instrument uses a total of 13 beam-defining apertures in order to avoid cross collimation (Brûlet *et al.*, 2008). The pre-sample enclosure is evacuated, while the post-sample vessel containing the neutron detector is filled with helium gas. The neutron guide sections upstream from the instrument produce a striped

(non-uniform) neutron beam cross section, as shown in Appendix *A*.

The neutron optics tests performed on this instrument used a nonstandard configuration with one (small) hole on the source (first) aperture and an array of equally spaced holes on the sample (last) aperture (aperture number 13). The remaining apertures (numbers 2 to 12, which are normally used to prevent cross collimation) were moved out of the neutron beam throughout these measurements, such that multiple spots were produced on the detector. Note that this instrument has been designed with the supermirror monochromator located between the first and second apertures. The distance between the two beam-defining apertures is l_1 = 2850 mm. The distance between the second beam-defining aperture and the sample position (where the lenses were located) is l = 880 mm. This gives a source-to-sample distance of $L_1 = l_1 + l$ = 3730 mm. The sample-to-detector distance is L_2 = 6078 mm. The radius of the (single-hole) source aperture is r_1 = 0.64 mm. The radius of each of the multiple holes on the second beam-defining aperture is r_2 = 0.45 mm, with center-to-center inter-hole distances a_x = 2.24 mm and a_y = 2.6 mm in the horizontal and vertical directions, respectively. Since this second beam-defining aperture is located at l = 880 mm before the sample position, these sample aperture sizes and distances are scaled to $r_2'' = 0.73$ mm, $a_x'' = 2.84$ mm and $a_y'' = 3.39$ mm on the basis of ray tracing simulation results (discussed in a later section). Such would have been the sizes of equivalent apertures located at the sample position. These estimated sizes and inter-hole distances agree well with simple geometric extrapolations.

A set of MgF_2 lenses (radius of curvature R = 25 mm, lens diameter of 25 mm with 1 mm thickness at the center) were positioned at the sample position; these were carefully aligned with respect to the neutron beam. Note that the neutron multi-beam diameter (14 mm) was smaller than the lens diameter. The total thickness for 30 lenses is close to 210 mm. Measurements were performed without lenses (N = 0) as well as with N = 30 lenses (this is close to the optimum focusing wavelength of $\lambda_0 = 14.76$ Å when the λ = 14.59 Å neutron wavelength was used) and with N = 18 lenses (way out of focus condition for which $\lambda_0 = 19.05$ Å). Measurements were undertaken using the four available neutron wavelengths when possible.

5. Variances of the neutron spot resolution

The two-dimensional data were processed in each case using the *OriginPro* data analysis software (http://originlab.com), whereby fits to a two-dimensional Gaussian function were performed for each beam spot:

$$I(x,y) = B + A\exp\left\{\frac{-\left[(x-x_c)\mu + (y-y_c)(1-\mu^2)^{1/2}\right]^2}{2\sigma_r^2} - \frac{\left[(x-x_c)(1-\mu^2)^{1/2} + (y-y_c)\mu\right]^2}{2\sigma_p^2}\right\}. \quad (13)$$

The fitting parameters are as follows: B is a constant background, A is the scale factor, x_c and y_c are the location coordinates of the spot center with respect to the neutron beam center, $\mu = \cos(\theta)$ (where θ is the orientation angle of the spot symmetry axis with respect to the horizontal x axis), and σ_r^2 and σ_p^2 are the radial and perpendicular spot variances.

Neutron optics measurements produced multiple spots on the high-resolution image-plate detector. When the lenses were used in the out-of-focus condition, these spots were elongated in the radial direction. Fig. 5 shows a typical image for the case with N = 30 lenses and λ = 12.34 Å. Since the neutron beam contains vertical stripes, locating the central spot required some effort. In order to determine precisely the central beam spot, two-dimensional fits to a series of spots in the horizontal and in the vertical directions were performed. The resulting spot variances were characterized by a minimum for each series corresponding to the central spot location. The resulting location of the central beam spot shown in Fig. 5 is consistent with the overall symmetry; stretching of the other spots with respect to that central location is evident.

The calculated and measured standard deviations for this case (N = 30 and λ = 12.34 Å) are compared in Fig. 6 for the horizontal direction and in Fig. 7 for the vertical direction. Lines representing polynomial fits are added as guides to the eye. The measured values are slightly different from the calculated ones, as expected, as a result of spurious scattering from lenses, windows and residual air in the neutron path. The measured perpendicular component was expected to be flat but turned out to contain curvature caused by the coupling between the radial and perpendicular components due to spurious scattering. The measured neutron beam turned out to be broader than the idealized one used in our analytical

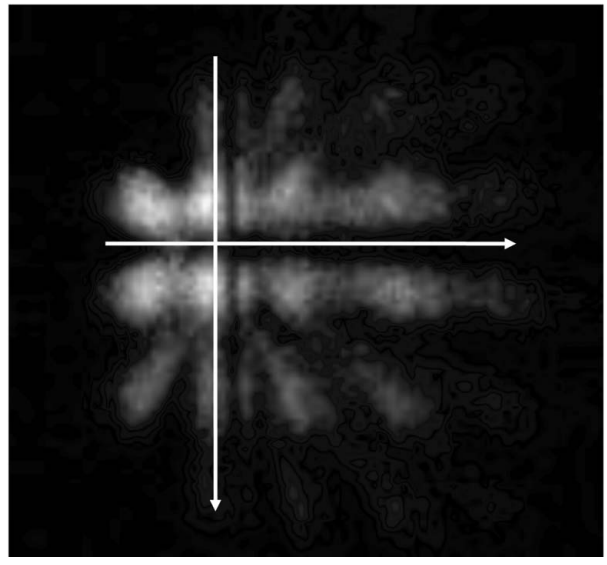

Figure 5
Neutron focusing test performed using N = 30 lenses and a neutron wavelength of λ = 12.34 Å. The arrows show the location of the beam center based on the analysis of series of spots in the horizontal and vertical directions. The directions of the arrows represent the data file format convention (note that y increases downward).

model. The minimum spot size corresponds to the central beam. Statistical error bars (obtained from fitting statistics) represent one standard deviation.

The data images without lenses and with 30 lenses are shown in Figs. 8 and 9, respectively, for the four neutron wavelengths. The case without lenses shows equally spaced spots with no distortion (Fig. 8), while the case with lenses shows a focusing effect (spots get closer) as well as spot distortion in the radial direction (Fig. 9). When no lenses are used, the variance of the spot sizes is essentially constant except for a small effect due to gravity at the longer wavelength.

Various measurements were made with different wavelengths and different numbers of lenses. A series of tests with the same neutron wavelength (12.34 Å) but an increasing number of lenses is included in Fig. 10.

The calculated and measured standard deviations for one of the spots (with indices $n_x = 1$ and $n_y = -2$) are plotted in Fig. 11 for increasing neutron wavelength. The available data sets corresponding to 30 lenses, 18 lenses and 0 lenses are included. Note that the case for 30 lenses and a wavelength of 14.59 Å is not included since all spots collapse to a single spot for the focusing wavelength. Data for 18 lenses at 6 and 9.1 Å are not available. The perpendicular component of the standard deviation does not change much except for the small gravity effect.

In order to compare the beam spot standard deviations when different numbers of lenses are used, the calculated radial component σ_r is plotted with varying λ/λ_0 for three

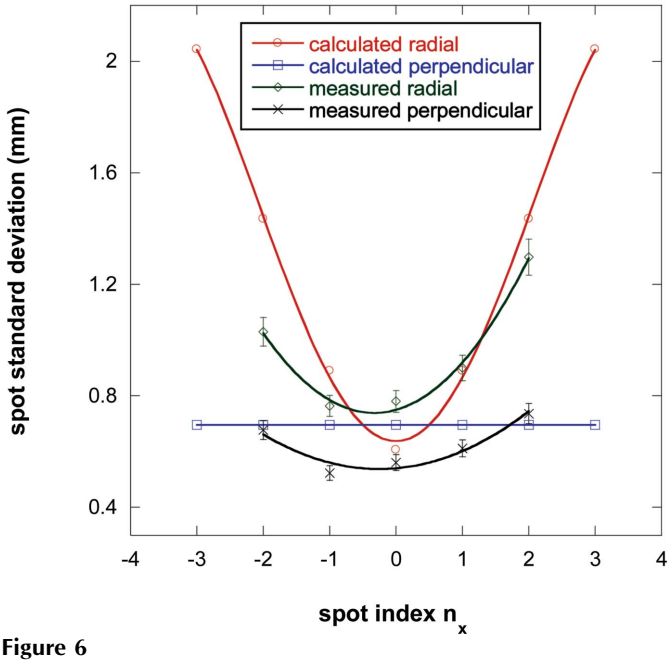

Figure 6
Neutron focusing test performed using N = 30 lenses and a neutron wavelength of λ = 12.34 Å. Comparison of the calculated and measured spot standard deviations in the radial and perpendicular directions for the horizontal series of spots (varying n_x).

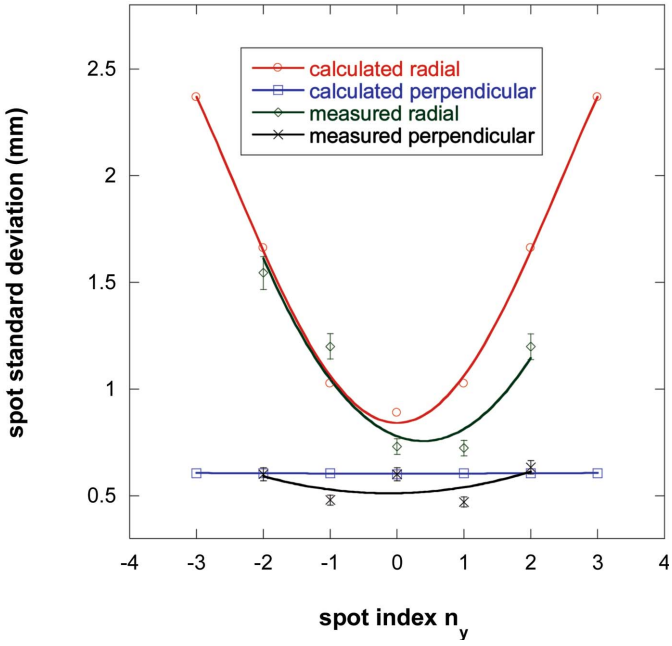

Figure 7
Neutron focusing test performed using N = 30 lenses and a neutron wavelength λ = 12.34 Å. Comparison of the calculated and measured standard deviations of the spot variances in the radial and perpendicular directions for the vertical series of spots (varying n_y).

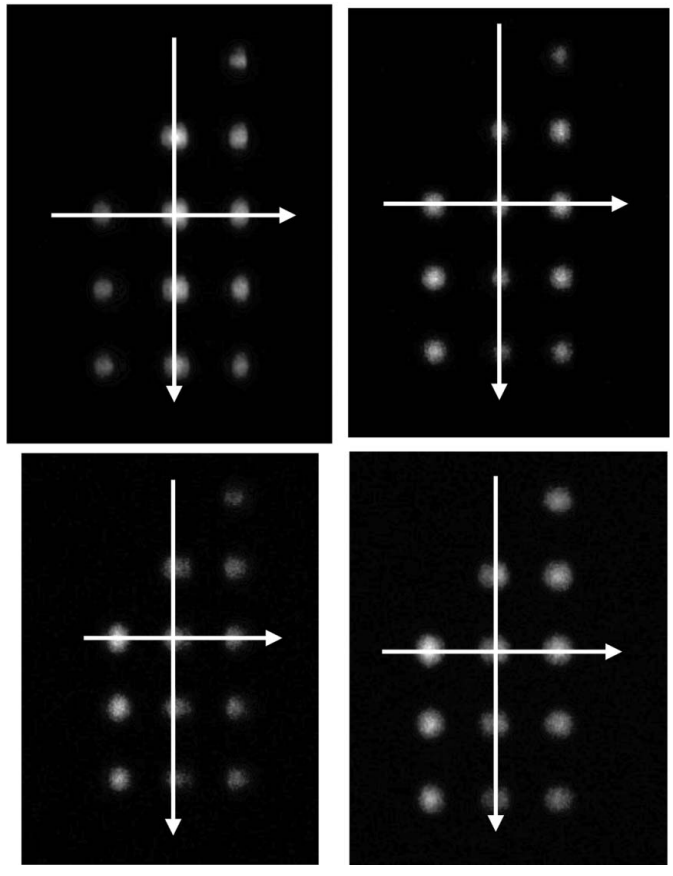

Figure 8
Neutron spots when no lenses are used. These correspond to neutron wavelengths of 6 Å (top left), 9.1 Å (top right), 12.34 Å (bottom left) and 14.59 Å (bottom right). Changing the wavelength does not change the spot geometry.

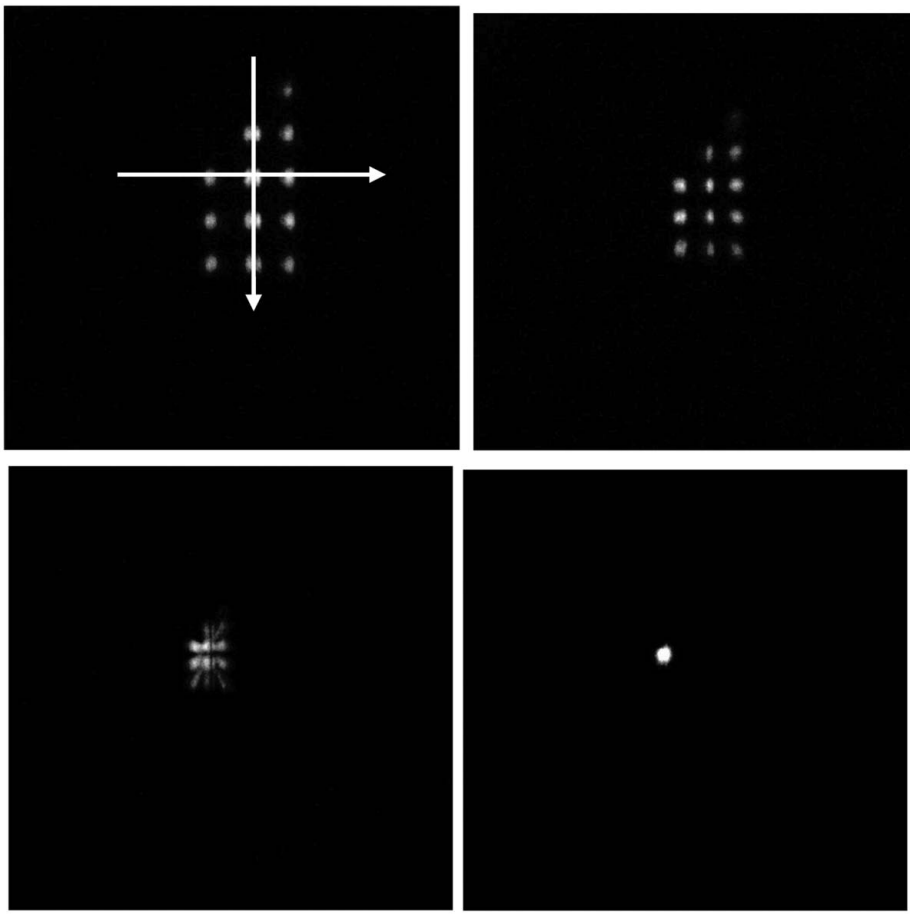

Figure 9
Neutron spots when 30 lenses are used. These correspond to neutron wavelengths of 6 Å (top left), 9.1 Å (top right), 12.34 Å (bottom left) and 14.59 Å (bottom right). Changing the wavelength focuses the various spots and distorts them along the radial direction. The last case showing a single spot corresponds to a wavelength of $\lambda = 14.59$ Å, which is close to the perfect focusing wavelength of $\lambda_0 = 14.76$ Å.

different off-axis beams, corresponding to ($n_x = 0$, $n_y = -2$), ($n_x = 1$, $n_y = -2$) and ($n_x = 1$, $n_y = 0$). Gravity contributes to the first two cases but not to the third one. The factor λ/λ_0 enters in two ways in the present formalism; it enters first in the sample term of the geometric contribution through the chromatic aberrations factor $S(\lambda, \lambda_0)$ [given in equation (7)], and second in the off-axis contribution that contains the beam index factor [see equation (11)]. The first contribution reduces the standard deviation when λ/λ_0 increases since $S(\lambda/\lambda_0 << 1) = 1$ and $S(\lambda = \lambda_0) = (2/3)(\Delta\lambda/\lambda)^2$ is very small, while the second contribution increases the standard deviation when λ/λ_0 increases. These two opposite contributions give the interesting effect whereby beam spots first shrink before expanding in the radial direction as λ/λ_0 increases, as shown in Fig. 12. This is, however, a small effect that is hard to observe experimentally with the data quality and resolution discussed here. The pure gravity effect represented by the term $-A\lambda^2$, which does not depend on (λ/λ_0), is small enough not to break the scaling behavior, as shown in Fig. 12.

Note that the use of multiple (small) holes on the source aperture increases the flux-on-sample and yields more symmetric spots on the detector. This is tantamount to an orientational averaging [averaging over the angle φ in equation (11)] which removes the anisotropy (spot elongation). The case of multiple holes on the source and sample apertures would yield multiple circular spots on the detector with standard deviations corresponding to the radial (*i.e.* elongated) component. Overkill apertures (used in the normal VSANS instrument operation but not used in these tests) would make all spots on the detector collapse to a single spot.

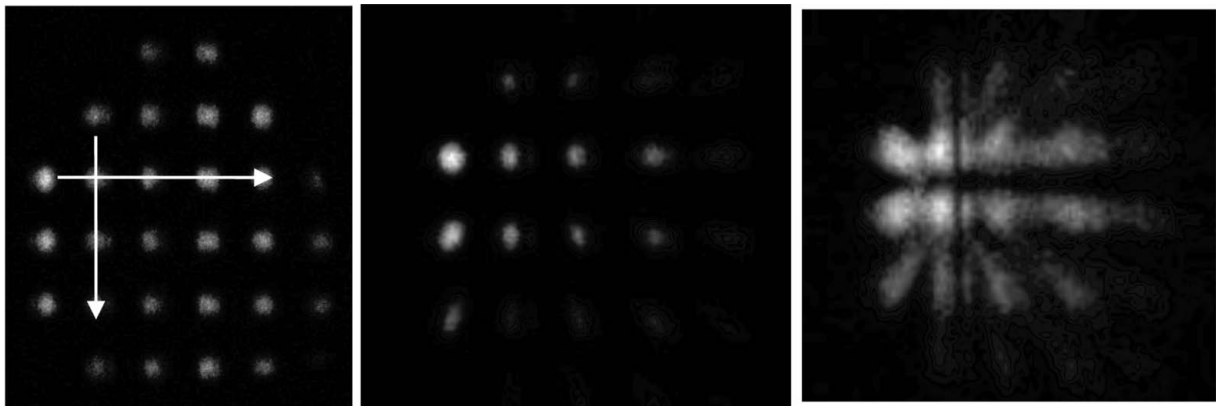

Figure 10
Neutron spots for a neutron wavelength of 12.34 Å and a varying number of lenses: $N = 0$ (left), $N = 18$ (center) and $N = 30$ (right).

6. Spot locations

Consider the transverse distance 'a' of an off-axis hole from the spectrometer axis on the sample aperture. In the absence of lenses, an image is formed at the detector position (at a distance L_2) from the sample aperture centered at a transverse location $a(1 + L_2/L_1)$. With the lens system, the image at the detector plane is formed at a transverse location $a(1 - L_2/L_4)$. From equation (5) this location becomes $a(1 + L_2/L_1) \times [1 - (\lambda/\lambda_0)^2]$. Consequently the location of the beam spot center for an off-axis hole $(n_x a_x, n_y a_y)$ is given by

$$\begin{aligned} \{x_c &= n_x a_x (1 + L_2/L_1) G(\lambda, \lambda_0), \\ y_c &= -A\lambda^2 + n_y a_y (1 + L_2/L_1) G(\lambda, \lambda_0)\}. \end{aligned} \tag{14}$$

The chromatic effects function $G(\lambda, \lambda_0)$ involves the averaging of $1 - (\lambda/\lambda_0)^2$ over the triangular wavelength distribution, which gives

$$G(\lambda, \lambda_0) = 1 - \left(\frac{\lambda}{\lambda_0}\right)^2 \left[1 + \frac{1}{6}\left(\frac{\Delta\lambda}{\lambda}\right)^2\right]. \tag{15}$$

Note that the proper limits are recovered for the in-focus and the no-lens conditions, respectively: $G(\lambda = \lambda_0) = -(1/6)(\Delta\lambda/\lambda)^2 = -(\sigma_\lambda/\lambda)^2$ and $G(\lambda, \lambda_0 \to \infty) = 1$. This function predicts the collapse of the various spots into one single spot when the focusing condition is reached (*i.e.* for $\lambda = \lambda_0$). Fig. 13 summarizes calculated and measured spot center locations for three of the four measured wavelengths when 30 lenses are used. The fourth wavelength of 14.59 Å corresponds closely to the in-focus condition (λ = 14.76 Å) whereby all spots collapse into a single one. A small (close to 6%) discrepancy between the calculated and measured results is observed for the 12.34 Å neutron wavelength. The other cases, corresponding to 6 and 9.1 Å wavelengths, agree well.

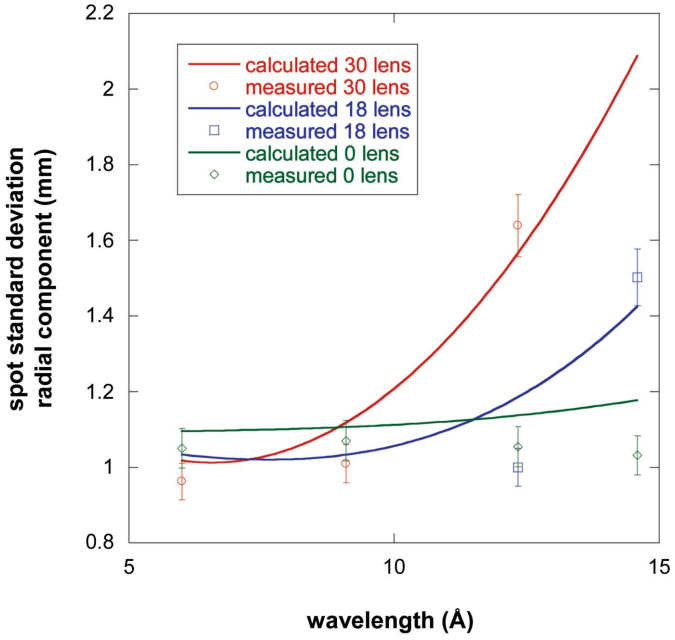

Figure 11
Variation of the calculated and measured standard deviations in the radial direction for one of the spots (with indices $n_x = 1$ and $n_y = -2$) for increasing neutron wavelength and a varying number of lenses. The $N = 0$ case corresponds to Fig. 8 and the $N = 30$ case corresponds to Fig. 9.

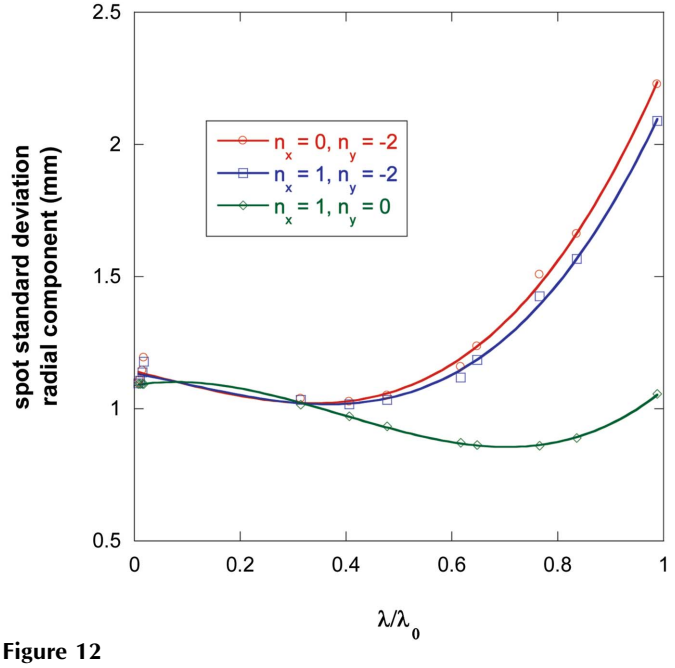

Figure 12
Variation of the neutron beam spot standard deviation (radial component) with varying λ/λ_0 for three different off-axis neutron beams. λ is the neutron wavelength and λ_0 is characteristic of the number N of lenses used (λ_0 = 14.76 Å for $N = 30$, λ_0 = 19.05 Å for $N = 18$ and $\lambda_0 = \infty$ for $N = 0$). The lines are polynomial fits added to show the trends.

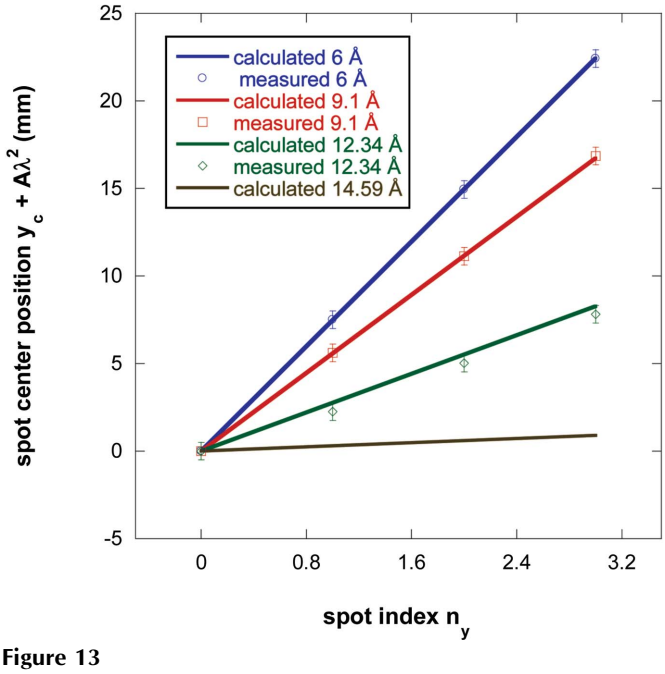

Figure 13
Comparing the measured and calculated spot center positions y_c at the detector position relative to the central hole position for 30 lenses for three of the measured neutron wavelengths (6, 9.1 and 12.34 Å). Beam spot positions obey the equation $y_c + A\lambda^2 = n_y a_y (1 + L_2/L_1) G(\lambda, \lambda_0)$. Since the 14.59 Å wavelength is very close to the focusing wavelength, all measured spots collapse to a single position, giving a line close to horizontal.

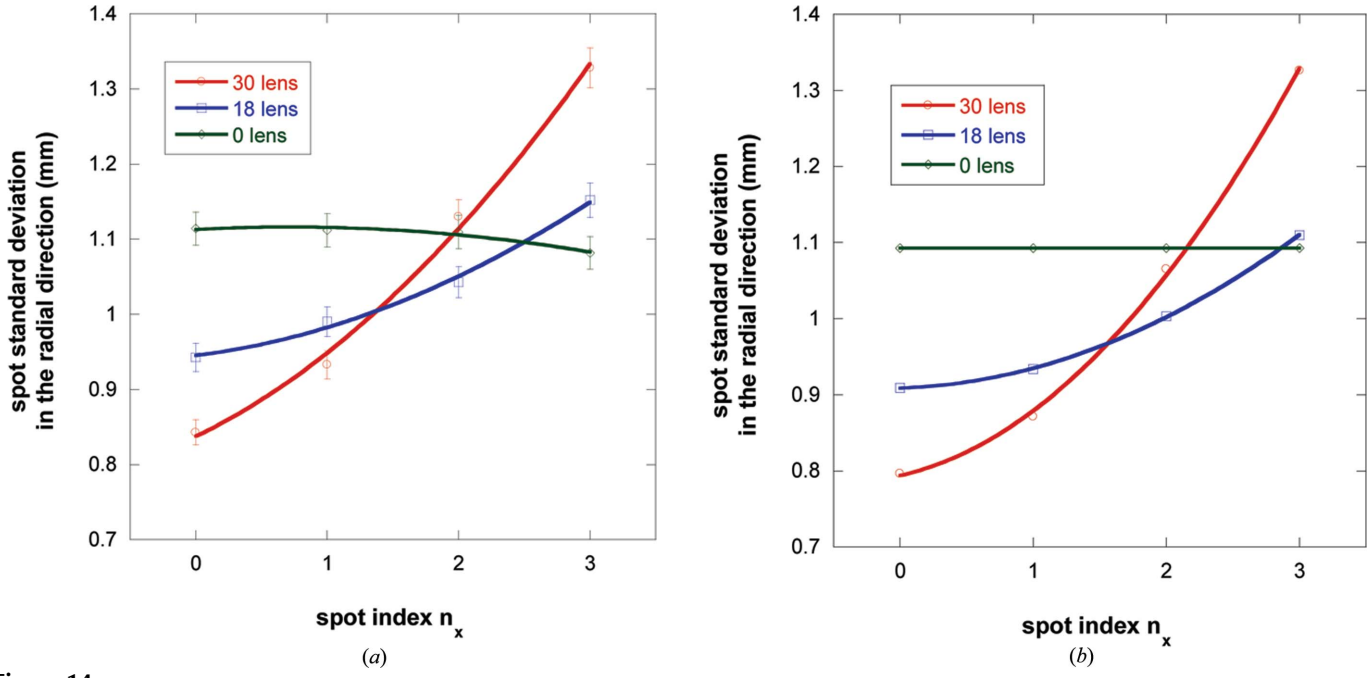

Figure 14
Simulation results (*a*) and analytical results (*b*) representing the standard deviation of the beam spot profile in the radial direction for the main (on-axis) beam and three off-axis beams for the 9.1 Å wavelength. The three cases of 30 lenses, 18 lenses and no lenses are plotted. Statistical error bars corresponding to one standard deviation have been included for the simulation results.

7. Ray tracing Monte Carlo simulation

We have used the ray tracing Monte Carlo simulation package *McStas* (Willendrup *et al.*, 2004; http://www.mcstas.org) to simulate neutron focusing for the conditions of our measurements. This package is readily available and is easy to use. Typical *McStas* commands are included in Appendix *B*.

A total of 10^8 neutrons (in each case) are sent down the collimation path; a good fraction of these neutrons make it to the detector. Simulation runs for some 3 min on a typical desktop computer (running windows) yield reliable results for each condition. Such results are compared with analytical calculations. Since the gravity effect is neglected in the *McStas* package that includes the focusing lenses software feature, only calculations in the horizontal **x** direction are considered.

In order to obtain an accurate comparison of the two methods (simulation and calculation), the standard deviations for the two-dimensional beam profiles of the various multi-spots on the detector are calculated by taking the square root of the second moment, $\sigma_x = \langle x^2 \rangle^{1/2} = \langle (x - \langle x \rangle)^2 \rangle^{1/2}$, where $\langle x \rangle$ is the average spot location. The analytical method also uses the second moment to calculate the standard deviation. Moments are calculated numerically by summing over each of the spots with detector counts as the weighing factor using the *OriginPro* software package.

The results from the two methods compare well, despite their respective advantages and drawbacks. The simulation method tends to overestimate the standard deviation when spots overlap as a result of neutron focusing, since it is hard to completely eliminate contributions from adjacent spots. The analytical method is, of course, approximate but yields a high accuracy level. Note the excellent agreement for the two methods with no neutron focusing (the zero-lens case). Emphasis is put on the radial direction since the perpendicular component is the same for all off-axis spots.

Fig. 14 compares the standard deviations for the three focusing cases (30 lenses, 18 lenses and 0 lenses) for the 9.1 Å wavelength in the radial direction. The analytical calculation method matches very well the no-lens case and reproduces the

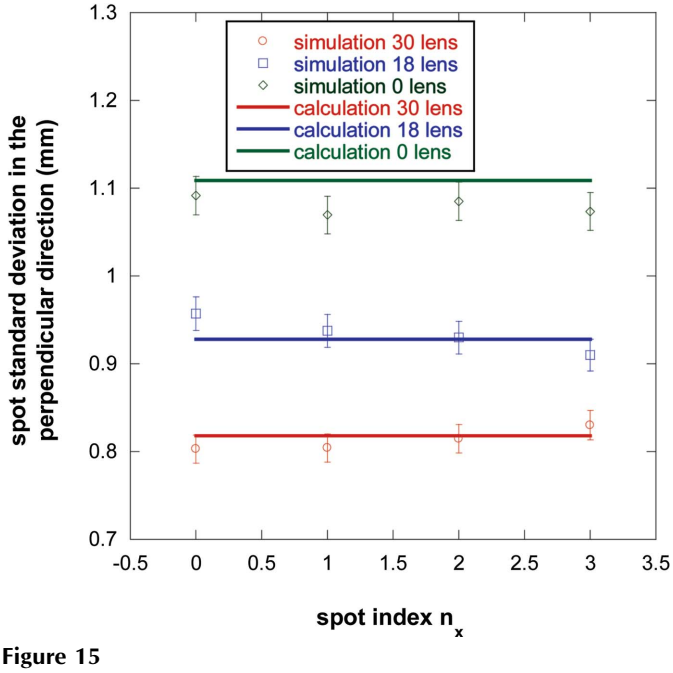

Figure 15
Simulation and analytical calculation results for the beam spot standard deviations in the perpendicular direction for the 9.1 Å wavelength.

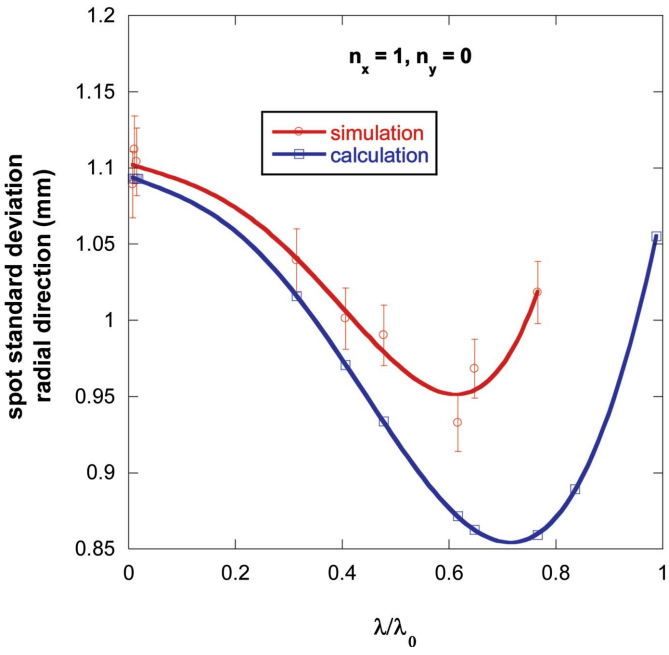

Figure 16
Comparison of the simulation and analytical calculation approaches plotted with increasing dimensionless parameter λ/λ_0 for spot ($n_x = 1, n_y = 0$).

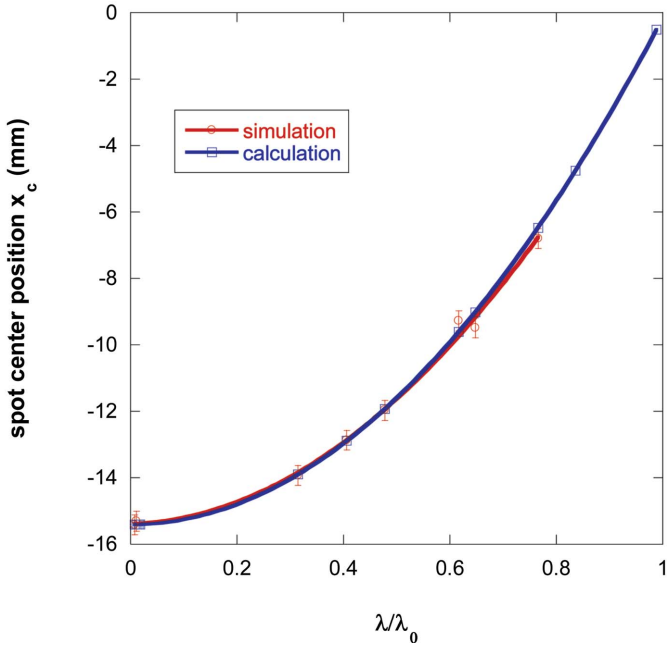

Figure 17
Comparison of the simulated and calculated spot center positions for most of the considered cases plotted against the dimensionless variable λ/λ_0. Beam spot positions obey the equation $x_c = n_x a_x(1 + L_2/L_1)G(\lambda, \lambda_0)$.

overall trend with lenses. There is room for refinement of the overall curved shape. Fig. 15 shows good agreements for the standard deviations in the perpendicular direction within statistical errors.

Fig. 16 compares the simulation and analytical calculation methods for most of the cases considered for spot ($n_x = 1, n_y = 0$). The horizontal axis represents the dimensionless variable λ/λ_0, where λ is the neutron wavelength and λ_0 is the focusing wavelength. Note that for 30 lenses $\lambda_0 = 14.75$ Å, for 18 lenses $\lambda_0 = 19.05$ Å, and for 0 lenses λ_0 is very large. The 30-lens case has not been included for $\lambda = 12.34$ and 14.59 Å wavelengths for the simulation approach since individual peaks cannot be resolved for these high-focusing conditions. The calculation approach tends to underestimate the spot standard deviations. Note that the trend reversal (standard deviation decreases then increases) predicted by the analytical calculation approach is confirmed by the simulation method. Lines through the points are polynomial fits included as guides to the eye.

Fig. 17 plots the spot center locations obtained as the first moment $x_c = \langle x \rangle$ in each case for both simulation and calculation. The agreement is rather good, as expected.

8. Summary and conclusions

We have developed a formalism to understand neutron focusing in the out-of-focus condition and for off-axis neutron beams. Neutron optics tests were performed on a VSANS instrument (TPA at Saclay) using a nonstandard configuration consisting of one single hole on the source aperture and an array of small (sub-millimetre radius) holes on the sample aperture. The high-resolution (0.15 mm) image-plate detector enabled the resolution of these individual neutron beams in detail. When focusing lenses are used, the off-axis spots become elongated in the radial direction. Data analysis consisted of nonlinear least-squares fits for each individual beam to a two-dimensional Gaussian function in order to obtain spot location coordinates and standard deviations in the radial and perpendicular directions. These were compared with model predictions. Despite the nonstandard experimental settings, enough agreement is found to give confidence in the neutron focusing formalism presented. Some of these non-typical experimental settings include a non-uniform neutron beam, a supermirror monochromator located between the beam-defining apertures (rather than before the source aperture), the location of the second beam-defining aperture some 880 mm before the sample position and the location of the lens system after the sample aperture. Simplifying assumptions made to develop the formalism (such as infinitely thin lenses, no spurious scattering from lenses, air *etc*) contribute to the observed discrepancy between calculated and measured beam standard deviations. The high-resolution image-plate neutron detector and the use of judicious beam-defining apertures with small (sub-millimetre radius) holes permit such measurements.

Furthermore, ray tracing Monte Carlo simulation was used to compare with analytical predictions for the various cases considered. Agreement was found between these two methods for the overall trends. The analytical calculation method tends to underestimate the standard deviation but reproduces the spot locations precisely. An interesting trend reversal (spot standard deviation in the radial direction decreases then increases) is noted as the neutron wavelength is increased. The reduction is due to chromatic aberrations in the sample term,

while the subsequent increase is due to the off-axis contribution to the chromatic effect. On the basis of the present findings, modeling of this last contribution could be improved with stronger wavelength dependence.

It should be stated that the results for the out-of-focus condition apply both to SANS and to VSANS, while the off-axis condition applies only to VSANS, since SANS instruments do not use multi-hole apertures.

APPENDIX *A*
Instrumental conditions

Additional instrumental conditions are included here. The image-plate neutron detector uses a scintillation plate that produces photons upon neutron absorption. Once a photon is produced, neutron detection becomes equivalent to X-ray detection. Europium-activated defect centers are excited when detection events are recorded. A laser is used to read out the recorded events (two-dimensional image), which are subsequently de-excited (zeroed out). This laser scanning process involves spinning the detector around its center. Reading is done at the end of each run. Image-plate data are recorded in a digital form.

Fig. 18 shows that the neutron guide sections upstream from the instrument produce a striped (non-uniform) neutron beam cross section. Note that these stripes are observed on the detector because the overkill apertures were not used in these tests. In normal VSANS operation, sample illumination is uniform.

APPENDIX *B*
McsStas commands

Typical *McStas* commands (included in an input file with extension `.instr`) are included here.

```
COMPONENT base = Arm() at (0,0,0) ABSOLUTE
```

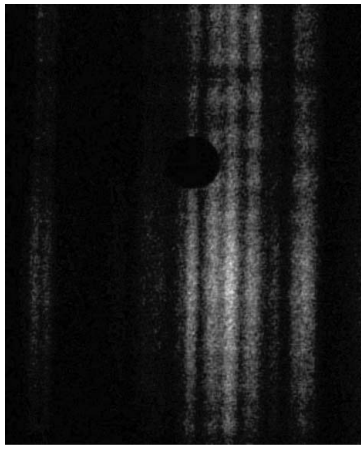

Figure 18
Portion of the neutron detector image with a source aperture only (no sample aperture). Guide sections upstream produce a striped neutron beam.

This component sets the origin from which absolute distances are measured along the neutron beam (in metres).

```
COMPONENT Source = Source_div(width = 0.0013,
height = 0.0013, hdiv = div, vdiv = div, Lambda0 =
lambda, dLambda = DeltaLambda) AT (0, 0, 0) RELATIVE
previous
```

This component defines the neutron source characteristics, such as wavelength, wavelength spread and beam divergence (in degrees), and is placed at the origin.

```
COMPONENT Aperture1 = Slit(radius = 0.00064) AT
(0, 0, 0) RELATIVE Source
```

This component places a source aperture (0.64 mm radius) also at the origin.

```
COMPONENT VelSel = Selector(xmin = -0.025, xmax =
0.025, ymin = -0.025, ymax = 0.025, len = 0.375334,
num = 47.6, width = 0.0006666, radius = 0.12, alfa =
48.298, feq = 96.86998) AT (0, 0, 0.001) RELATIVE
previous
```

This component insets a velocity selector to obtain a triangular wavelength distribution.

```
COMPONENT Aperture13 = RomSlit(file = 'FenteTPA13.
txt') AT (0, 0, 2.850) RELATIVE Source
```

This component places a multi-hole mask some 2.85 m downstream. Hole sizes and inter-hole spacings are included in a file called `FenteTPA13.txt`.

```
COMPONENT LensPos = lenses(d = 0.025, e = 0.001,
r1 = 0.025, r2 = 0.025, N = N) AT (0, 0, 3.73)
RELATIVE Source rotated(0, 0, 0) relative previous
```

This component describes the set of focusing lenses used; their curvature diameter, thickness, radius, the number of lenses and their location along the beam.

```
COMPONENT Detector3 = PSD_monitor(nx = 200, ny =
200, filename = 'TPAlens3.txt', xwidth = 0.030,
yheight = 0.030) AT (0, 0, 9.808) RELATIVE Source
```

This last component records neutron beam counts on a fictitious detector located 9.8 m downstream from the source. The total detector area is 3×3 cm, containing 200×200 cells, yielding a detector resolution of 0.15 mm in each direction. The detector is located at the same location as the neutron detector during the neutron focusing (experimental) measurements. Locating this detector at a fictitious location at the sample position yields an estimate for the beam spot at the sample position when the beam-defining aperture is located some 880 mm upstream.

The identification of commercial products does not imply endorsement by the National Institute of Standards and Technology nor does it imply that these are the best for the purpose. This work is based upon activities supported in part by the National Science Foundation under agreement No. DMR-0944772. Partial financial support of BH by CE Saclay during his one-month research leave there is appreciated. This research project has been supported by the European Commission under the 7th Framework Programme through the 'Research Infrastructures' action of the 'Capacities Programmme' (contract No. CP-CSA_INFRA-2008-1.1.1 226507-NMI3). Help from Vincent Thévenot is appreciated.

References

Brûlet, A., Thévenot, V., Lairez, D., Lecommandoux, S., Agut, W., Armes, S. P., Du, J. & Désert, S. (2008). *J. Appl. Cryst.* **41**, 161–166.

Choi, S.-M., Barker, J. G., Glinka, C. J., Cheng, Y. T. & Gammel, P. L. (2000). *J. Appl. Cryst.* **33**, 793–796.

Désert, S., Thévenot, V., Gabriel, A., Permingeat, P., Oberdisse, J. & Brûlet, A. (2007). *J. Appl. Cryst.* **40**, 945–949.

Eskildsen, M. R., Gammel, P. L., Issacs, E. D., Detlefs, C., Mortensen, K. & Bishop, D. J. (1998). *Nature*, **391**, 563–566.

Gähler, R., Kalus, J. & Mampe, W. J. (1980). *Phys. E Sci. Instrum.* **13**, 546–548.

Hammouda, B. & Mildner, D. F. R. (2007). *J. Appl. Cryst.* **40**, 250–259.

Mildner, D. F. R. (2005). *J. Appl. Cryst.* **38**, 488–492.

Mildner, D. F. R. & Carpenter, J. M. (1984). *J. Appl. Cryst.* **17**, 249–256.

Mildner, D. F. R., Hammouda, B. & Kline, S. R. (2005). *J. Appl. Cryst.* **38**, 979–987.

Willendrup, P., Farhi, E. & Lehmann, K. (2004). *Physica B*, **350**, E735–E737.